A statistical damage model for bone tissue based on distinct compressive and tensile cracks

A statistical damage model for bone tissue based on distinct compressive and tensile cracks

Philippe K. Zysset[1], Jakob Schwiedrzik & Uwe Wolfram

Institute for Surgical Technology and Biomechanics,
University of Bern, Switzerland
Laboratory for Mechanics of Materials and Nanostructures,
Swiss Federal Laboratories for Materials Science and Technology, Switzerland
Institute for Mechanical, Process and Energy Engineering,
Heriot-Watt University, United Kingdom

Abstract

Osteoporosis leads to bone fragility and represents a major health problem in our aging societies. Bone is a quasi-brittle hierarchical composite that exhibits damage with distinct crack morphologies in compression and tension when overloaded. A recent study reported the complex damage response of bovine compact bone under four different cyclic overloading experiments combining compression and tension. The aim of the present work is to propose a mechanistic model by which cracking bone accumulates residual strain and reduces elastic modulus in distinct compressive and tensile overloading modes. A simple rheological unit of bone with two types of cracks is formulated in the framework of continuum damage mechanics. A statistics of these rheological units is then assembled in parallel to compute the response of a macroscopic bone sample in which compressive and tensile cracks are opened, closed or propagated towards failure. The resulting constitutive model reproduces the key macroscopic features of bone tissue damage and delivers an excellent agreement with the four cyclic overloading experiments. The remarkable predictions of the model

[1]Email address of corresponding author: philippe.zysset@istb.unibe.ch

support the presence of 1) friction between the crack surfaces producing hystereses, 2) an incomplete closure of cracks leading to residual strains, 3) a bridging mechanism of collagen fibrils which failure reduces elastic modulus, and 4) two distinct classes of cracks where compressive cracks have a strong influence on tensile damage and tensile cracks have a limited impact on compressive damage. This work is expected to help improve our understanding of the bone damage mechanisms contributing to skeletal fragility and to foster a proper generalization of this damage behavior in 3D for computational analysis of bone and bone-implant systems.

Number of words: abstract=268 and article=3388 (without equations, references and captions)

Keywords: Bone, Constitutive Model, Damage, Micro-cracks, Residual Strain, Rheological Model, Strength

1. Introduction

In our aging societies, the growing incidence of osteoporotic bone fractures motivates a refined exploration not only of bone mechanical properties as a function of age and disease, but also in bone loading during physiological activities or accidental situation such as falls.

Bone is a hierarchical, heterogeneous and anisotropic composite that exhibits a quasi-brittle damage mode at the macro-scale that consists of accumulation of residual strains and a reduction in elastic modulus due to micro-cracks (Fondrk et al., 1999; Taylor et al., 2007; Garcia et al., 2009). Despite organizational differences at the bone structural unit level, a similar damage behavior is

observed in trabecular and compact bone tissue, which points to the same underlying micro-cracking mechanism of the extracellular matrix (Keaveny et al., 1994; Fazzalari et al., 1998; Lambers et al., 2013). At the nanoscale, deformation of bone is determined by mineralized collagen fibrils interacting through a thin interfibrillar glue layer (Fratzl and Weinkamer, 2007), which represents an ideal interface for initiation of residual shear strains, progressive sliding of mineralized fibril bundles, formation of diffuse damage (Zioupos et al., 1994; Poundarik et al., 2012), and coalescing into micro-cracks (Frost, 1960; Lee et al., 2003).

Micro-damage is partly repaired by self-healing mechanisms (Seref-Ferlengez et al., 2014) and the cell-orchestrated remodeling process (Burr et al., 1985), but is believed to be at least partially responsible for the reduced toughness of bone with age (Zimmermann et al., 2011). From a biomechanical perspective, increasing attention is therefore devoted to elucidate the role of micro-damage on the various post-yield properties of bone tissue.

Rate-independent rheological models to describe the reduction of elastic modulus and accumulation of residual strains of trabecular bone were proposed and even generalized to 3D in the framework of continuum damage mechanics (Zysset and Curnier, 1996; Garcia et al., 2009). Two distinct dissipation processes are responsible for the friction between crack surfaces producing residual strains and the growth of cracks reducing elastic modulus. Rate-dependent constitutive models were also proposed for compact bone (Garcia et al., 2010; Fondrk et al., 1999), but remain to a large extent phenomenological and were not able to describe the interaction between compressive and tensile damage.
In a pioneering work based on a parallel arrangement of linear elastic spring elements undergoing brittle failure beyond a given ultimate strain, Krajcinovic et al. (1987) described successfully the reduction of elastic modulus as well

as stress softening of cortical bone in tension. This model was motivated by the parallel arrangement of osteons in the bone microstructure and the overall compact bone strength emerged from a uniform statistics of element strengths. Although in a compressive loading mode, two recent experimental studies on dry micro-samples could confirm that the strength of the bone extracellular matrix is substantially higher than the strength of macroscopic osteonal bone samples (Schwiedrzik et al., 2014; Luczynski et al., 2015). Moreover, Schwiedrzik et al. (1987) reported large residual strains and no damage in their micro-samples. Applying the statistical distribution idea of Krajcinovic et al. (1987) to elasto-plastic rheological elements, they could not only predict the observed scale effect in longitudinal bone strength but also the apparition of damage and stress softening at the macro-scale.

Motivated by the different loading modes of osteoporotic bones in physiological versus traumatic conditions, a recent experimental study investigated the impact of damage accumulated in tension and compression on the other deformation mode in bovine osteonal bone (Mirzaali et al., 2015). Histological examination confirmed that tensile damage consists mostly of diffuse cracks that were oriented perpendicular to the osteonal loading axis, while compression resulted in more contrasted cross-hatched cracks that were oriented at 45° with respect to the osteonal axis (Reilly and Currey, 1999). After tensile damage, compressive loading closes the perpendicular cracks (Sun et al., 2010) and their influence on the subsequent elastic and post-yield behavior in compression was found to be limited. In contrast, the shear damage accumulated under uniaxial compression had a significant influence on the elastic and post-yield behavior in tension. This interaction between compressive and tensile loading cannot be explained by the statistical model of (Schwiedrzik et al., 2014) devoted exclusively to compression.

Accordingly, the aim of the present work was to generalize our previous rheological model to include the damage behavior produced under tension that is able to describe qualitatively and quantitatively the asymmetric coupling effects observed in the cyclic tests of Mirzaali et al. (2015). The paper is divided in sections describing the proposed rheological unit, the assembly of a statistics of unit models, the identification of the material constants combined with the results and a discussion. The actual numerical algorithm to compute the model's response is provided in the appendix. The study of such constitutive models is expected to contribute to the understanding of the damage mechanisms underlying bone fragility and to inspire the development of improved 3D constitutive models for FE analysis of bone and bone-implant systems.

2. Rheological model

In this section, a single unit model is developed that will then be assembled in section 3 into a statistics of units with specific distributions of material properties. The single unit model (Fig. 1) consists of a linear elastic spring representing the intact bone extracellular matrix in series with two crack elements representing each a distinct compression and tension crack that can open and close but not beyond a given closure strain illustrated by a stop. Each crack is modeled by a rate-independent slider in parallel with a spring representing the collagen fibrils bridging the crack. The tension and compression sliders have high frictional stress thresholds in the opening mode and much lower thresholds in the closing mode. The collagen springs fail beyond a given ultimate strain. Beyond this ultimate strain, the frictional behavior of the sliders vanishes as well and, due to its perpendicular configuration, only the stop of the closing tensile crack remains effective. The series arrangement of the model leads to an additive

decomposition of the elastic and crack strains:

$$E = E^e + E^c + E^t \tag{1}$$

where the compressive crack strain E^c and the tensile crack strain E^t are independent internal variables. The same crack strains E^c and E^t are relevant for stretching of the bridging collagen fibrils. The series arrangement implies also that the total stress is identical in the matrix and in the crack.

Bone tissue is made of bundles of mineralized collagen fibrils arranged in series and parallel and can therefore be represented by a statistics of such rheological models. The post-yield behavior in compression and tension is then driven by two families of cracks that generate residual strains, reduce elastic modulus by failing of the bridging collagen fibrils and dissipate energy in both processes.

In the standard generalized materials framework, a free energy ψ provides the stresses associated with the reversible springs and a dual dissipation potential ϕ^* delivers the evolution or flow rules of the internal variables, namely the residual strains and the damage variables responsible for failure of the bridging collagen fibrils and vanishing of the frictional forces. These two functions and the stresses are presented in the next subsections followed by the resulting flow rules.

2.1. Free energy

The free energy of the model represents the sum of the recoverable energy stored in the extracellular matrix and in the collagen fibers bridging the two cracks:

$$\psi = \psi^e(E, E^c, E^t) + \psi^c(E^c, D^c) + \psi^t(E^t, D^t) \tag{2}$$

The free energy of the intact matrix is

$$\psi^e(E, E^c, E^t) = \frac{1}{2}\epsilon(E - E^c - E^t)^2 \tag{3}$$

where ϵ is Young's modulus.

The free energy related to the bridging of collagen fibrils in the compression crack is

$$\psi^c(E^c, D^c) = \begin{cases} \frac{1}{2}(1 - D^c)\chi^c {E^c}^2 + I_{]-\infty,0]}(E^c) & \text{if } D^c < 1 \\ 0 & \text{if } D^c = 1 \end{cases} \tag{4}$$

where χ^c is the hardening modulus and $D^c \in [0, 1]$ is a damage variable that reduces the modulus of the spring (Lemaitre and Chaboche, 1990). The indicatrix function is defined by

$$I_{\{.\}}(X) = \begin{cases} 0 & \text{if } X \in \{.\} \\ +\infty & \text{otherwise} \end{cases}$$

The latter function ensures that strain of the compression crack remains positive until failure ($D^c < 1$). However, as shown in Fig. 1, this restriction vanishes at failure and the strain of the compression crack can become positive when $D^c = 1$.

The free energy related to the the bridging of collagen fibrils (ligaments) in the tensile crack is

$$\psi^t(E^t, D^t) = \frac{1}{2}(1 - D^t)\chi^t {E^t}^2 + I_{[E^{t,clo},+\infty[}(E^t) \tag{5}$$

where χ^t is the hardening modulus, $D^t \in [0, 1]$ is a damage variable that breaks the tensile spring and $E^{t,clo} \geq 0$ is a positive closure strain of the tensile crack

that grows linearly with maximal crack opening:

$$E^{t,clo}(t) = \gamma Max_{\tau\in[0,t]}\{E^t(\tau)\} \geq 0 \tag{6}$$

where $\gamma > 0$ is the proportionality factor.

Unlike sliding of compression cracks, closing of tensile cracks remains limited by $E^{t,clo}$ when $D^t = 1$. This is justified by the perpendicular configuration of tensile cracks that close and lock in compression even when the collagen spring is failed and no friction can occur any more.

The total stress S is given by the derivative of the free energy with respect to the total strain

$$S = \frac{\partial \psi}{\partial E} = \epsilon(E - E^c - E^t) \tag{7}$$

The frictional stress S^c in the compression crack slider also derives from the free energy with respect to the compressive crack strain,

$$\begin{aligned} S^c &\in -\partial_{E^c}\psi \\ &\in \begin{cases} \begin{cases} \{\epsilon(E - E^c - E^t) - (1 - D^c)\chi^c E^c\} & \text{if } E^c < 0 \\ [\epsilon(E - E^t), +\infty[& \text{if } E^c = 0 \\ \emptyset & \text{if } E^c > 0 \end{cases} & \text{if } D^c < 1 \\ \{0\} & \text{if } D^c = 1 \end{cases} \end{aligned} \tag{8}$$

where $\partial_x\psi$ is the sub-differential of ψ with respect to the variable x that generalizes the derivative to non-differentiable (C^0) functions (Rockafellar, 1970). The symbol $\emptyset$ is the empty set.

The second frictional stress S^t of the tensile slider derives from the free energy

with respect to the tensile crack strain,

$$\begin{aligned} S^t &\in -\partial_{E^t}\psi \\ &\in \begin{cases} \emptyset & \text{if } E^t < E^{t,clo} \\ ]-\infty, \epsilon(E - E^c - E^{t,clo})] & \text{if } E^t = E^{t,clo} \\ \{\epsilon(E - E^c - E^t) - (1 - D^t)\chi^t E^t\} & \text{if } E^t > E^{t,clo} \end{cases} \end{aligned} \tag{9}$$

Similarly, the conjugate energies to the two damage variables are obtained from derivation of the free energy:

$$W^c = -\frac{\partial \psi}{\partial D^c} = \frac{1}{2}\chi^c E^{c2} \tag{10}$$

$$W^t = -\frac{\partial \psi}{\partial D^t} = \frac{1}{2}\chi^t E^{t2} \tag{11}$$

2.2. Dual dissipation potential

In the framework of standard generalized materials, the flow rules of the internal variables, here the residual strains and damage variables, derive from a dual dissipation potential ϕ^* depending on the conjugate variables. For a rate-independent process, the dissipation potential is the indicatrix of the convex set representing the flow criterion (Germain, 1973). Due to the independence of the internal variables and their conjugates, the dissipation potential can be expressed as the sum of independent contributions:

$$\phi^* = \phi^{*,E^c}(S^c; E^c, D^c) + \phi^{*,E^t}(S^t; E^t) + \phi^{*,D^c}(W^c) + \phi^{*,D^t}(W^t)$$

where the variables listed after the semi-colon are considered as parameters. The compression part responsible for crack opening and closing is

$$\phi^{*,E^c} = \left\{ \begin{array}{ll} \left\{ \begin{array}{ll} I_{[-\sigma^{c-},+\sigma^{c+}]}(S^c) & \text{if } E^c < 0 \\ I_{[-\sigma^{c-},+\infty[}(S^c) & \text{if } E^c = 0 \\ \emptyset & \text{if } E^c > 0 \end{array} \right. & \text{if } D^c < 1 \\ \left\{ \{0\} \right. & \text{if } D^c = 1 \end{array} \right. \tag{12}$$

where σ^{c-} and σ^{c+} are the absolute values of the stress thresholds for opening and closing of the compression crack. The tensile part is

$$\phi^{*,E^t} = \left\{ \begin{array}{ll} \emptyset & \text{if } E^t < E^{t,clo} \\ I_{]-\infty,+(1-D^t)\sigma^{t+}]}(S^t) & \text{if } E^t = E^{t,clo} \\ I_{[-(1-D^t)\sigma^{t-},+(1-D^t)\sigma^{t+}]}(S^t) & \text{if } E^t > E^{t,clo} \end{array} \right. \tag{13}$$

where σ^{t-} and σ^{t+} are the stress thresholds for closing and opening of the tensile cracks. The compressive and tensile crack failure parts are

$$\phi^{*,D^c} = I_{[0,W^{c,ult}]}(W^c) \tag{14}$$

$$\phi^{*,D^t} = I_{[0,W^{t,ult}]}(W^t) \tag{15}$$

2.3. Flow rules

The flow rule resulting for the compression crack strain is

$$\dot{E}^c \in \partial_{S^c}\phi^{*,E^c} = \begin{cases} \begin{cases} \emptyset & \text{if } S^c < -\sigma^{c-} \\ ]-\infty, 0] & \text{if } S^c = -\sigma^{c-} \\ \{0\} & \text{if } S^c \in]-\sigma^{c-}, +\sigma^{c+}[\\ [0, +\infty[& \text{if } S^c = +\sigma^{c+} \\ \emptyset & \text{if } S^c > +\sigma^{c+} \end{cases} & \text{if } E^c < 0 \\ \begin{cases} \emptyset & \text{if } S^c < -\sigma^{c-} \\ ]-\infty, 0] & \text{if } S^c = -\sigma^{c-} \\ \{0\} & \text{if } S^c \in]-\sigma^{c-}, +\infty[\end{cases} & \text{if } E^c = 0 \end{cases} \tag{16}$$

For the strain variable related to the tensile crack

$$\dot{E}^t \in \partial_{S^t}\phi^{*,E^t} = \begin{cases} \begin{cases} \emptyset & \text{if } S^t < -(1-D^t)\sigma^{t-} \\ ]-\infty, 0] & \text{if } S^t = -(1-D^t)\sigma^{t-} \\ \{0\} & \text{if } S^t \in]-(1-D^t)\sigma^{t-}; (1-D^t)\sigma^{t+}[\\ [0, +\infty[& \text{if } S^t = (1-D^t)\sigma^{t+} \\ \emptyset & \text{if } S^t > (1-D^t)\sigma^{t+} \end{cases} & \text{if } E^t > E^{t,clo} \\ \begin{cases} \{0\} & \text{if } S^t \in]-\infty; (1-D^t)\sigma^{t+}[\\ [0, +\infty[& \text{if } S^t = (1-D^t)\sigma^{t+} \\ \emptyset & \text{if } S^t > (1-D^t)\sigma^{t+} \end{cases} & \text{if } E^t = E^{t,clo} \end{cases} \tag{17}$$

Similarly, the flow rule for the corresponding damage variables become

$$\dot{D}^c \in \partial_{W^c}\phi^{*,D^c} = \begin{cases} \emptyset & \text{if } W^c < 0 \\ \{0\} & \text{if } W^c \in [0; W^{c,ult}[\\ [0, +\infty[& \text{if } W^c = W^{c,ult} \\ \emptyset & \text{if } W^c > W^{c,ult} \end{cases} \tag{18}$$

and

$$\dot{D}^t \in \partial_{W^t}\phi^{*,D^t} = \begin{cases} \emptyset & \text{if } W^t < 0 \\ 0 & \text{if } W^t \in [0; W^{t,ult}[\\ [0, +\infty[& \text{if } W^t = W^{t,ult} \\ \emptyset & \text{if } W^t > W^{t,ult} \end{cases} \tag{19}$$

Since the damage criteria are constant values of an elastic energy function W that increases monotonically with strain, the failure of the crack elements becomes fully brittle. The definition of the conjugate energies implies that their ultimate values correspond to ultimate crack strains:

$$W^{c,ult} = \frac{1}{2}\chi^c (E^{c,ult})^2 \Rightarrow E^{c,ult} = -\sqrt{\frac{2W^{c,ult}}{\chi^c}} \tag{20}$$

$$W^{t,ult} = \frac{1}{2}\chi^t (E^{t,ult})^2 \Rightarrow E^{t,ult} = \sqrt{\frac{2W^{t,ult}}{\chi^t}}. \tag{21}$$

The latter flow rules determine entirely the mechanical behavior of the rheological model and the numerical implementation of these flow rules is presented in the appendix. The power dissipated by the model is the sum of the specific dissipative processes

$$\Phi = S^c \dot{E}^c + S^t \dot{E}^t + W^c \dot{D}^c + W^t \dot{D}^t. \tag{22}$$

The first two terms relate to friction associated with residual strains in compression and tension, while the two last terms are related to failure of the collagen springs and the associated annealing of the frictional resistance.

2.4. Response of the single element model

The response of the developed single element model under cyclic loading is illustrated in Fig. 2. The dissipative loops in compression and tension correspond to opening and closing of the respective compression and tensile cracks. Failure of the tensile crack ($D^t = 1$) still allows for compressive stresses, but failure of the compression crack ($D^c = 1$) brings the total stress of the model to zero everywhere. An animation of the rheological model's response is provided in the supplementary material.

3. Statistics of elements

The behavior of bone tissue is then represented by a statistics of rheological elements arranged in parallel. Following our previous work on micro-pillar compression (Schwiedrzik et al., 2014), distinct statistical distributions were assigned to the conservative and dissipative material properties. The elastic properties of the extracellular matrix and the bridging springs follow a normal distribution with a relative standard deviation of 8%, while the yield stresses and ultimate crack strains follow a uniform distribution up to a maximal value (Fig. 3). Given the strain formulation adopted in the above theory, computing the response of the model requires only total stress for a strain based experiment, but requires also the total tangent operator necessary in the numerical implementation for a stress driven experiment.

Due to the parallel configuration of the rheological elements, the converged

stresses and the tangent operators are simply added:

$$S_{i+1}^{tot} = \sum_{e=1}^{nele} S_{i+1}^{e} \tag{23}$$

$$\frac{dS_{i+1}^{tot}}{dE_{i+1}} = \sum_{e=1}^{nele} \frac{dS_{i+1}^{e}}{dE_{i+1}} \tag{24}$$

where *nele* is the number of elements.

4. Identification of material constants and results

The material constants were determined from the different experimental curves for bovine bone obtained by Mirzaali et al. (Table **??**). The monotonic experiments delivered directly the crack opening stresses, hardening slopes and ultimate strains in compression and tension, while a trial and error process with the cyclic experiments provided the closing stresses as well as the residual closure strain in tension. The number of elements was set to 240 as a compromise between smoothness of the response and computing time. A convergence analysis up to 1920 elements for monotonic tension and compression was conducted that confirmed that beyond 240 elements, the mean stress errors over the entire stress-strain curves remained below 1% (Fig. 4). The response of the model to the monotonic experiments in compression and tension is displayed in Fig. 4. As expected, the opening stress amplitude and the ultimate strain of tensile cracks is significantly lower than the ones of compression cracks, which leads to the well known difference in tensile and compressive ultimate strength of bone. In compression, progressive failure of the elements lead to a slight reduction of stress (stress softening) beyond a maximal value. In tension, the post-yield response is almost constant up to 1.5% strain due to the higher hardening slope of the bridging spring.

The loading schedule, stress response, numerical and experimental stress-strain curves of a cyclic experiment in compression is shown in Fig. 5. The statistical model captures the key features of the compressive damage process, namely the residual strains, the reduction in stiffness due to failure of the bridging collagen fibrils and the hysteresis produced by opening and closing of the cracks. Clearly, the damage accumulated in compression becomes visible in the response to the interrogation cycles in tension where stiffness is progressively reduced.

The same illustration is shown in Fig. 6 for a cyclic experiment in tension. Again, the residual strains, stiffness reduction and hysteresis are properly reproduced by the numerical simulation. In contrast to the previous cyclic experiment, the response to the interrogation cycles in compression do not reveal the presence of any reduction in compressive stiffness. A small shift of the tensile crack closure strains $E^{t,clo}$ improves the qualitative correspondence with the experimental curves.

The loading schedule, stress response, numerical and experimental stress-strain curves of a further cyclic experiment in compression followed by a monotonic loading in tension is shown in Fig. 7. Beyond the proper account of the damage process in compression, the model predicts the induced reduction in tensile strength.

The same illustration is shown in Fig. 8 for the cyclic experiment in tension followed by a monotonic loading in compression. The post-yield behavior in compression remains essentially unchanged after the overloading in tension.

Finally, the obtained material constants fulfill the equations 1 (Appendix), and suggest that closure of tensile cracks require proportionally more stress than closure of compression cracks. Animations of the cyclic load cases are provided in the supplementary material.

5. Discussion

The aim of this work was to formulate, program and evaluate a novel constitutive model to describe the influence of compressive and tensile crack families on the cyclic response of bone tissue at the macroscopic level. A minimal set of 10 material constants was determined with six types of experimental curves in monotonic compression, tension and multiple combinations of loading cycles. In monotonic compression and tension, the distinct opening stresses and hardening slopes are sufficient to reproduce the experimental stress-strain curves both qualitatively and quantitatively. Interestingly, the post-yield material constants obtained here by fitting the macroscopic monotonic compression curves for bovine compact bone ($\sigma^{c-} = 456$ MPa and $E^{c,ult} = 0.07$) are in the same range as the ones found for micro-pillar compression experiments for a single crack in ovine bone ($\sigma^{c-} = 521$ MPa and $E^{c,ult} = 0.08$) (Schwiedrzik et al., 2014).

In cyclic compressive overload, the model predicts also the macroscopic residual strain, the reduction in elastic modulus and the growing hysteresis in a repeated loading/unloading cycle (Fig. 5). The tensile damage is clearly visible with the reduction in elastic modulus and the ultimate strength in tension is strongly degraded (Fig. 7).

In cyclic tensile overload, the model predicts the macroscopic residual strain, the reduced modulus and the progressing hysteresis (Fig. 6). In the absence of substantial compressive loading, compressive damage remains low as only very few elements yield and fail in compression. The ultimate strength in compression remains essentially unaffected (Fig. 8).

The remarkable correspondence of the experimental and simulation stress-strain curves (Fig. 5 - Fig. 8) suggests that the hypotheses of the model are consistent

with the actual bone damage process at the micro-scale.

First, friction between the crack surfaces leads to hystereses in the cyclic stress-strain diagrams and represents an important dissipative mechanism that tends to increase with growing damage as more cracks are open. The distinct level of friction in the opening and closing modes may well be the rheological manifestation of the sacrificial molecular bonds observed in AFM studies (Fantner et al., 2005). Second, the residual strains observed at the macroscopic level in the absence of load emerge from the incomplete closure of the cracks in both compression and tension mode. Moreover, the tensile crack strain do not return to zero even after a compression cycle indicating that potentially some debris pushed between the crack surfaces may prevent the tensile cracks to close completely. Third, propagation of a crack through the ECM unit and the subsequent failure of the bridging collagen fibrils is responsible for the reduced elastic modulus observed in cyclic experiments and recovers the original idea of (Krajcinovic et al., 1987). Fourth, compression and tensile cracks have indeed a distinct mechanical behavior related to their orientation in the bone microstructure with respect to the loading direction. The yield stress is three times higher in compression than in tension, which is partially compensated by an order of magnitude higher hardening slope in tension to achieve a macroscopic ultimate stress that is 85% higher in compression than in tension. The higher hardening slope induces also a more monotonic post-yield curve in tension (Fig. 4). The different nature of the stop in compression and tension cracks explains not only the reduction of the modulus in tension after accumulation of damage in compression, but also the insensitivity of the modulus in compression after damage accumulated in tension.

Despite the successful qualitative and quantitative predictions of the uniaxial bone response for rather complex loading sequences, the model has some limi-

tations. First, the response of the bridging collagen fibrils was assumed to be linear and neither viscoelasticity, nor viscous damage was included. In principle, linear or non-linear dampers could be added in the ECM and in parallel to each crack, but a proper identification would require a large number of experiments performed at different strain rates on similar samples. More importantly, this 1D model is limited to uniaxial loading along the osteonal axis and was not identified along other grain directions that are likely to deliver substantially different material constants since toughness was shown to be substantially lower for cracks along the osteonal axis (Peterlik et al., 2006). Also, no shear loading was investigated. Finally, the presented model is based on a continuum approach of damage and cannot describe the propagation of the failing crack treated in fracture mechanics.

The initial motivation for this model was to assess the potential weakening of the proximal femur in a side fall configuration due to damage accumulation in a physiological loading mode associated with normal activities. Femoral bone tissue loaded in tension or compression during a fall may indeed be loaded in the opposite mode during gait. What we learn from our findings is that the compressive damage accumulated in the medial cortex during stance will indeed be detrimental to the overloading in tension caused by a fall on the side (Nawathe et al., 2014). In contrast, the tensile damage that may accumulate in the supero-lateral cortex would hardly affect the mechanical resistance against overloading in compression due to a fall. This qualitative deduction calls obviously for further research as the amount and distribution of micro-damage in the human osteoporotic proximal femur is widely unknown.

Nevertheless, the main benefits of such models are their relative simplicity and their capacity to explain macroscopic behavior from a statistics of mechanical prototypes (Bazant, 2004).The proposed model including crack opening and

closing is well-suited to extend quasi-static damage to fatigue damage and this will be the object of future developments. Full generalization of this model to 3D including anisotropy may prove to become difficult, but may be of high interest for realistic computational analysis of bones and bone-implant systems subjected to cyclic loading. In the light of the identified cracking mechanisms, it becomes clear that the widely used elasto-plastic models are not appropriate for bone as soon as unloading histories are involved. Finally, the understanding of damage accumulation history in a human skeleton's life and its repair by self-healing and bone remodeling remains a major challenge in contemporary bone research.

Acknowledgments

This work was supported by grant no 143769 of the Swiss National Science Foundation (SNF) and the start-up grant S-12-13W of the AO foundation. The authors acknowledge Mohammad Mirzaali for realizing the challenging mechanical tests.

Conflicts of interest statement

The authors have no conflicts of interest to disclose.

References

Bazant, Z. P., 2004. Scaling theory for quasibrittle structural failure. Proc Natl Acad Sci USA 101 (37), 13400–13407.

Burr, D., Martin, R., Schaffler, M., Radin, E., 1985. Bone remodeling in response to in vivo fatigue microdamage. Journal of Biomechanics 18 (3), 189–200.

Curnier, A., 1994. Computational Methods in Solid Mechanics. Springer, Dordrecht.

Fantner, G.E., Hassenkam, T., Kindt, J. H., Weaver, J. C., Birkedal, H., Pechenik, L., Cutroni, J. A., Cidade, G. A., Stucky, G. D., Morse, D. E., Hansma, P. K., 2005. Sacrificial bonds and hidden length dissipate energy as mineralized fibrils separate during bone fracture. Nature Material 4 (8), 612–616.

Fazzalari, N., Forwood, M., Manthey, B., Smith, K., Kolesik, P., 1998. Three-dimensional confocal images of microdamage in cancellous bone. Bone 23 (4), 373–378.

Fondrk, M., Bahniuk, E., Davy, D., 1999. Inelastic strain accumulation in cortical bone during rapid transient tensile loading. Journal of Biomechanical Engineering 121, 616–621.

Fratzl, P., Weinkamer, R., 2007. Nature's hierarchical materials. Progress in Materials Science 52, 1263–1334.

Frost, H., 1960. Presence of microcracks in vivo in bone. Henry Ford Hospital Medical Bulletin 8, 25–35.

Garcia, D., Zysset, P. K., Charlebois, M., Curnier, A., 2009. A three-dimensional elastic plastic damage constitutive law for bone tissue. Biomechanics and Modeling in Mechanobiology 8 (2), 149–65.

Garcia, D., Zysset, P., Charlebois, M., Curnier, A., 2010. One-dimensional elastic plastic damage constitutive law for cortical bone. Archive of Applied Mechanics 80 (5), 543–555.

Germain, P., 1973. Cours de mécanique des milieux continus. Vol. 1. Masson, Paris.

Keaveny, T., Guo, X., Wachtel, E., McMahon, T., Hayes, W., 1994. Trabecular bone exhibits fully linear elastic behaviour and yields at low strains. Journal of Biomechanics 27, 1127–1136.

Krajcinovic, D., Trafimow, J., Sumarac, D., 1987. Simple constitutive model for cortical bone. Journal of Biomechanics 20, 779–784.

Lambers, F. M., Bouman, A. R., Rimnac, C. M., Hernandez, C. J., 2013. Microdamage caused by fatigue loading in human cancellous bone: relationship to reductions in bone biomechanical performance. PLoS One 8 (12), e83662.

Lee, T. C., Mohsin, S., Taylor, D., Parkesh, R., Gunnlaugsson, T., O'Brien, F. J., Giehl, M., Gowin, W., 2003. Detecting microdamage in bone. Journal of Anatomy 203 (2), 161–72.

Lemaitre, J., Chaboche, J.-L., 1990. Mechanics of solid materials. Cambridge University Press.

Luczynski, K. W., Steiger-Thirsfeld, A., Bernardi, J., Eberhardsteiner, J., Hellmich, C., 2015. Extracellular bone matrix exhibits hardening elastoplasticity and more than double cortical strength: Evidence from homogeneous

compression of non-tapered single micron-sized pillars welded to a rigid substrate. Journal of the Mechanical Behavior of Biomedical Materials.

Mirzaali, M. J., Burki, A., Schwiedrzik, J., Zysset, P. K., Wolfram, U., 2015. Continuum damage interactions between tension and compression in osteonal bone. Journal of the Mechanical Behavior of Biomedical Materials 49, 355–69.

Nawathe, S., Akhlaghpour, H., Bouxsein, M. L., Keaveny, T. M., 2014. Microstructural failure mechanisms in the human proximal femur for sideways fall loading. J Bone Miner Res 29 (2), 507–15.

Peterlik, H., Roschger, P., Klaushofer, K., Fratzl, P., 2006. From brittle to ductile fracture of bone. Nature Materials 5 (1), 52–5.

Poundarik, A. A., Diab, T., Sroga, G. E., Ural, A., Boskey, A. L., Gundberg, C. M., Vashishth, D., 2012. Dilatational band formation in bone. Proc Natl Acad Sci USA 109 (47), 19178–83.

Reilly, G. C., Currey, J. D., 1999. The development of microcracking and failure in bone depends on the loading mode to which it is adapted. The Journal of Experimental Biology 202, 543–552.

Rockafellar, R., 1970. Convex analysis. Princeton University Press.

Schwiedrzik, J., Raghavan, R., Burki, A., LeNader, V., Wolfram, U., Michler, J., Zysset, P., 2014. In situ micropillar compression reveals superior strength and ductility but an absence of damage in lamellar bone. Nature Materials 13 (7), 740–7.

Seref-Ferlengez, Z., Basta-Pljakic, J., Kennedy, O. D., Philemon, C. J., Schaffler, M. B., 2014. Structural and mechanical repair of diffuse damage in cortical bone in vivo. Journal of Bone and Mineral Research 29 (12), 2537–44.

Sun, X., Hoon Jeon, J., Blendell, J., Akkus, O., 2010. Visualization of a phantom post-yield deformation process in cortical bone. J Biomech 43 (10), 1989–96.

Taylor, D., Hazenberg, J. G., Lee, T. C., 2007. Living with cracks: damage and repair in human bone. Nature Materials 6 (4), 263–8.

Zimmermann, E. A., Schaible, E., Bale, H., Barth, H. D., Tang, S. Y., Reichert, P., Busse, B., Alliston, T., Ager, J. W., r., Ritchie, R. O., 2011. Age-related changes in the plasticity and toughness of human cortical bone at multiple length scales. Proc Natl Acad Sci USA 108 (35), 14416–21.

Zioupos, P., Currey, J. D., Sedman, A. J., 1994. An examination of the micromechanics of failure of bone and antler by acoustic emission tests ans laser scanning confocal microscopy. Medical Engineering and Physics 16, 203–213.

Zysset, P. K., Curnier, A., 1996. A 3d damage model for trabecular bone based on fabric tensors. J Biomech 29 (12), 1549–58.

6. Appendix: Numerical algorithm

This appendix provides the detailed algorithm to reprogram the proposed single element rheological model. Knowing the internal variables at the previous time step n, the algorithm of a strain based method aims at calculating the total stress S_{n+1} and the update of the internal variables for a given new total strain E_{n+1}. In the alternative case of a stress based approach, an iterative method is used to estimate a new strain E_{i+1} that requires additionally the tangent operator dS_{i+1}/dE_{i+1}. At convergence of the iterative method, $E_{n+1} = E_{i+1}$ and the strain variables are updated accordingly. For a detailed insight in these classical concepts, see for instance (Curnier, 1994).

6.1. Hypothesis

We first assume here that 1) the crack opening stress in compression is strictly lower than the crack closing stress in tension, and 2) the crack opening stress in tension is strictly higher than the crack closing stress in compression:

$$-\sigma^{c-} < -\sigma^{t-} \qquad \sigma^{t+} > \sigma^{c+} \tag{1}$$

where all material constants σ are positive real numbers. These conditions are consistent with the experimental observations at the macroscopic scale and ensure that only one crack strain evolves at a given time in the model. Both conditions are maintained with respect to a change in the crack closure strains $E^{t,clo} > 0$.

6.2. Failed compression crack

If the damage variable $D_n^c = 1$ then the total stress

$$S_{i+1} = 0 \tag{2}$$

and the tangent stiffness

$$\frac{dS_{i+1}}{dE_{i+1}} = 0 \tag{3}$$

The algorithm stops here for that element and the variables $D_{n+1}^c = 1$, $E_{n+1}^c = E_{n+1}$ and $E_{n+1}^t = 0$ are updated at convergence.

6.3. Trial stresses

If the damage variable $D_n^c = 0$, trial stresses $S^{c,trial}$ and $S^{t,trial}$ are computed that depend on the crack strains E_n^c, E_n^t and tensile damage D_n^t of the previous

time step:

$$S_{i+1}^{c,trial} = \epsilon(E_{i+1} - E_n^c - E_n^t) - \chi^c E_n^c \tag{4}$$

$$S_{i+1}^{t,trial} = \epsilon(E_{i+1} - E_n^c - E_n^t) - (1 - D_n^t)\chi^t E_n^t \tag{5}$$

6.3.1. Elastic case

In case no yield criterion is active

$$S_{i+1}^{c,trial} > -\sigma^{c-} \qquad and \qquad S_{i+1}^{c,trial} < \sigma^{c+} \tag{6}$$

$$S_{i+1}^{t,trial} < (1 - D_n^t)\sigma^{t+} \qquad and \qquad S_{i+1}^{t,trial} > -(1 - D_n^t)\sigma^{t-} \tag{7}$$

The response is elastic

$$S_{i+1} = \epsilon(E_{i+1} - E_n^c - E_n^t) \tag{8}$$

and the tangent is

$$\frac{dS_{i+1}}{dE_{i+1}} = \epsilon \tag{9}$$

Since no flow occurs, all internal variables are updated with their value at the previous time step.

6.3.2. Compression crack opening

If $S_{i+1}^{c,trial} \leq -\sigma^{c-}$, the following projection is performed:

$$E_{i+1}^c = \frac{\epsilon(E_{i+1} - E_n^t) + \sigma^{c-}}{\epsilon + \chi^c} \tag{10}$$

The resulting stress remains

$$S_{i+1} = \epsilon(E_{i+1} - E^c_{i+1} - E^t_n) \tag{11}$$

The corresponding tangent is

$$\frac{dS_{i+1}}{dE_{i+1}} = \frac{\epsilon\chi^c}{\epsilon + \chi^c} \tag{12}$$

The update will enforce $E^c_{n+1} = E^c_{i+1}$ and $E^t_{n+1} = E^t_n$.

In case the failure threshold is attained,

$$E^c_{n+1} \leq E^{c,ult} \Rightarrow D^c_{n+1} = 1 \tag{13}$$

6.3.3. Compression crack closing

If $S^{c,trial}_{i+1} \geq +\sigma^{c+}$, the following projection is performed:

$$E^c_{i+1} = Min(0, \frac{\epsilon(E_{i+1} - E^t_n) - \sigma^{c+}}{\epsilon + \chi^c}) \tag{14}$$

The minimum ensures that the compression crack does not close beyond the zero strain.

The resulting stress is

$$S_{i+1} = \epsilon(E_{i+1} - E^c_{i+1} - E^t_n) \tag{15}$$

If $E^c_{i+1} = 0$, the tangent is

$$\frac{dS_{i+1}}{dE_{i+1}} = \epsilon \tag{16}$$

else

$$\frac{dS_{i+1}}{dE_{i+1}} = \frac{\epsilon\chi^c}{\epsilon + \chi^c} \tag{17}$$

The update will enforce $E^c_{n+1} = E^c_{i+1}$ and $E^t_{n+1} = E^t_n$.

6.3.4. Tension crack opening

Then, if $S^{t,trial}_{i+1} \geq (1 - D^t_n)\sigma^{t+}$, the other projection is performed:

$$E^t_{i+1} = \frac{\epsilon(E_{i+1} - E^c_n) - (1 - D^t_n)\sigma^{t+}}{\epsilon + (1 - D^t_n)\chi^t} \tag{18}$$

The total stress remains

$$S_{i+1} = \epsilon(E_{i+1} - E^c_n - E^t_{i+1}) \tag{19}$$

The tangent is

$$\frac{dS_{i+1}}{dE_{i+1}} = \frac{\epsilon(1 - D^t_n)\chi^t}{\epsilon + (1 - D^t_n)\chi^t} \tag{20}$$

The update will enforce $E^t_{n+1} = E^t_{i+1}$ and $E^c_{n+1} = E^c_n$.

Finally, if the residual strain at convergence exceeds the failure threshold

$$E^t_{n+1} \geq E^{t,ult} \Rightarrow D^t_{n+1} = 1 \tag{21}$$

6.3.5. Tension crack closing

Then, if $S^{t,trial}_{i+1} \leq -(1 - D^t_n)\sigma^{t-}$, the alternative projection is performed:

$$E^t_{i+1} = Max(E^{t,clo}, \frac{\epsilon(E_{i+1} - E^c_n) + (1 - D^t_n)\sigma^{t-}}{\epsilon + (1 - D^t_n)\chi^t}) \tag{22}$$

The maximum ensures that the crack does not close beyond the limit strain $E^{t,clo}$.

The total stress is

$$S_{i+1} = \epsilon(E_{i+1} - E^c_n - E^t_{i+1}) \tag{23}$$

If $E^t_{i+1} = E^{t,clo}$

$$\frac{dS_{i+1}}{dE_{i+1}} = \epsilon \tag{24}$$

else

$$\frac{dS_{i+1}}{dE_{i+1}} = \frac{\epsilon(1 - D^t_n)\chi^t}{\epsilon + (1 - D^t_n)\chi^t} \tag{25}$$

The update will enforce $E^t_{n+1} = E^t_{i+1}$ and $E^c_{n+1} = E^c_n$.

Tables

Exp./ Samples	Variables Units	ϵ [MPa]	χ [MPa]	σ^- [MPa]	σ^+ [MPa]	E^{ult} [-]	γ [-]
Fig. 2	ECM	21′700	–	–	–	–	–
Fig. 2	Comp. crack	–	543	456	64	0.070	–
Fig. 2	Tension crack	–	5′425	76	152	0.035	0.12
Fig. 4 L	ECM	24′000	–	–	–	–	–
Fig. 4 L	Comp. crack	–	600	432	43	0.085	–
Fig. 4 L	Tension crack	–	6′000	84	168	0.035	0.12
Fig. 4 R	ECM	22′500	–	–	–	–	–
Fig. 4 R	Comp. crack	–	600	473	47	0.070	–
Fig. 4 R	Tension crack	–	6′000	85	169	0.035	0.12
Fig. 5	ECM	30′000	–	–	–	–	–
Fig. 5	Comp. crack	–	7′500	270	49	0.020	–
Fig. 5	Tension interface	–	7′500	105	210	0.035	0.12
Fig. 6	ECM	26′000	–	–	–	–	–
Fig. 6	Comp. crack	–	650	546	98	0.070	–
Fig. 6	Tension crack	–	6′500	68	195	0.030	0.30
Fig. 7	ECM	21′700	–	–	–	–	–
Fig. 7	Comp. crack	–	543	260	26	0.050	–
Fig. 7	Tension crack	–	5′425	38	76	0.040	0.12
Fig. 8	ECM	17′000	–	–	–	–	–
Fig. 8	Comp. crack	–	425	405	20	0.046	–
Fig. 8	Tension crack	–	4′250	61	122	0.028	0.12

Table 1: Material constants for the three components of the rheological model used in Fig. 2 and the six experiments/samples shown in Fig. 4-8. The letters "L" and "R" stand for left and right.

Figure Captions

Figure 1: Top: Rheological model of a linear elastic bone matrix (spring) with compression and tension cracks that can open and close (sliders) with bridging collagen fibrils (kinematic hardening) and locking mechanisms (stops) in the opposite loading mode. When the sliders reach the open end of the support, the crack elements reach an ultimate strain and undergo brittle failure. Bottom: Stress-strain behavior of the three rheological elements for two loading cycles with increasing amplitudes. The spring (E^e) shows linear elasticity, while the compression crack (E^c) and the tension crack (E^t) exhibit plasticity with kinematic hardening followed by brittle failure beyond the ultimate strains ($E^{c,ult}$ and $E^{t,ult}$). The crack models exhibit distinct flow stresses in compression ($\sigma^{c\pm}$) and tension ($\sigma^{t\pm}$) but undergo locking in the opposite loading mode as long as they do not fail. The position of the tensile stop increases with the maximal extension strain. Upon brittle failure (dotted lines), the compression crack does not carry stress in any mode ($D^c = 1$), while the tensile crack can still sustain compressive stress ($D^t = 1$).

Figure 2: Response of the single element model to cyclic loading with increasing amplitudes. The tensile crack shows a strong hardening slope, while opening of the compression crack requires a higher stress amplitude. Failure is only partial in extension as it can still sustain load in shortening but the failure becomes complete beyond a given shortening threshold. An animation of the loading and stress-strain curves is available in the supplementary material.

Figure 3: Parallel arrangement of rheological elements with statistical distribution of parameters. The elastic parameters of the ECM and the collagen fibrils are distributed normally, while the yield and failure parameters are assigned a uniform distribution.

Figure 4: Response of the model to monotonic compression (left) and monotonic tension (right). In black, the experimental curves from (Mirzaali et al., 2015) and in blue with increasing intensity, the simulation curves with 120, 240, 480, 960 and 1920 elements. Mean changes in stress remain below 1% beyond n=240. In compression, the ultimate stress is about 190 MPa and the ultimate strain approximately 0.015. In tension, the yield stress is approximately 90 MPa and no ultimate strain can be defined. The enhanced ductility in tension is due to the higher hardening slope. The material constants were adapted to the two experimentally tested bovine bone samples (see Table 1) and kept identical for the convergence study.

Figure 5: Response of the model to cyclic compression. In the upper left graph, the applied strain schedule and below the resulting stress. In the upper right graph, the experimental stress-strain curve from (Mirzaali et al., 2015) and below the simulation curve in dark blue superimposed to the experimental curve in light gray. The overloading in compression produces substantial damage in tension. The material constants were adapted to the tested bone sample and provided in Table 1.

Figure 6: Response of the model to cyclic tension. In the upper left graph, the applied strain schedule and below the resulting stress. In the upper right graph, the experimental stress-strain curve from(Mirzaali et al., 2015) and below the simulation curve in dark blue superimposed to the experimental curve in light gray. The overloading in tension produces essentially no damage in compression, but the cracks do not close completely. The material constants were adapted to the tested bone sample and provided in Table 1.

Figure 7: Response of the model to cyclic compression followed by monotonic tension. In the upper left graph, the applied strain schedule and below the resulting stress. In the upper right graph, the experimental stress-strain curve from(Mirzaali et al., 2015) and below the simulation curve in dark blue superimposed to the experimental curve in light gray. The ultimate stress in tension is substantially reduced by damage in compression. The material constants were adapted to the tested bone sample and provided in Table 1.

Figure 8: Response of the model to cyclic tension followed by monotonic compression. In the upper left graph, the applied strain schedule and below the resulting stress. In the upper right graph, the experimental stress-strain curve from(Mirzaali et al., 2015) and below the simulation curve in dark blue superimposed to the experimental curve in light gray. The ultimate stress in compression is not influenced by damage in tension. The material constants were adapted to the tested bone sample and provided in Table 1.

Figure
Click here to download Figure: Fig1.eps

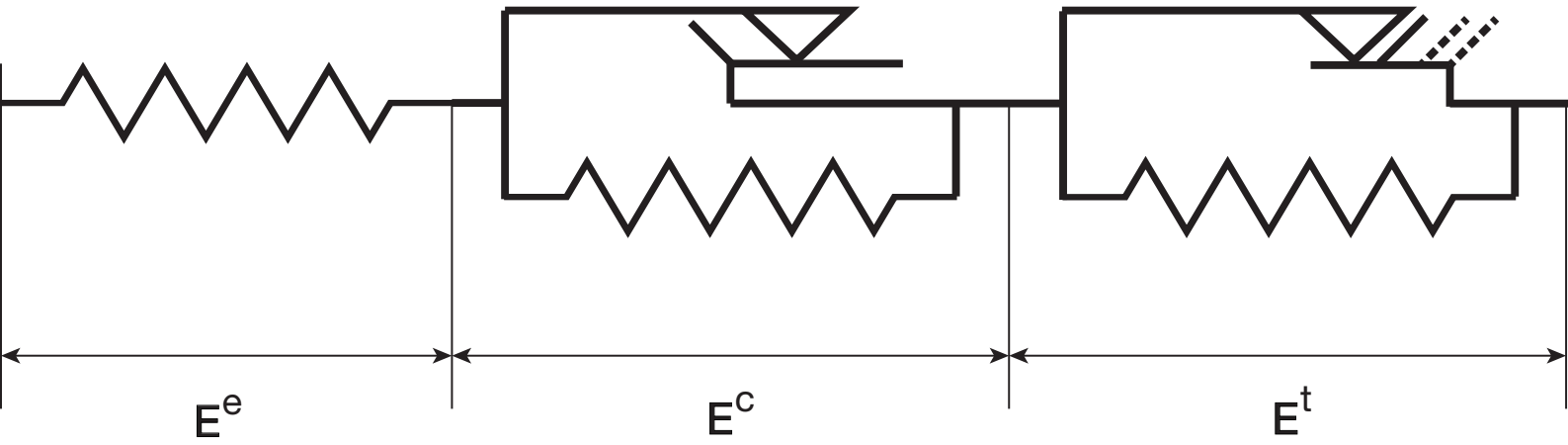

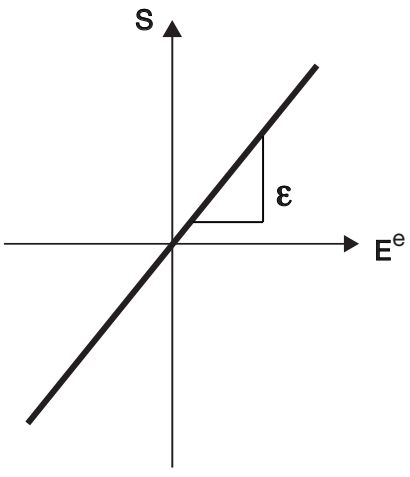

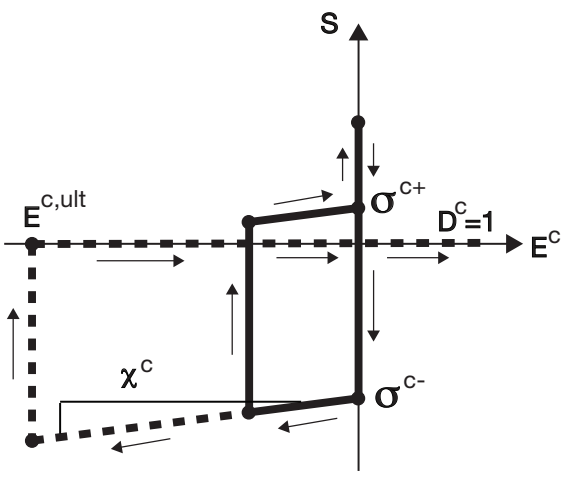

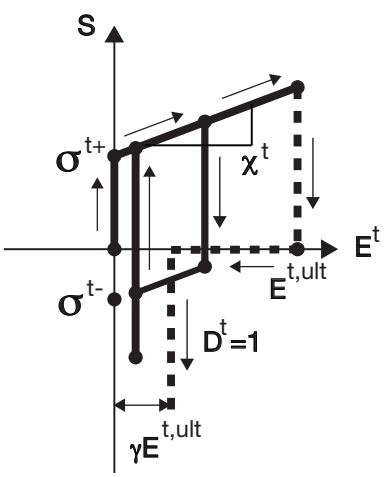

Figure
Click here to download Figure: Fig2.eps

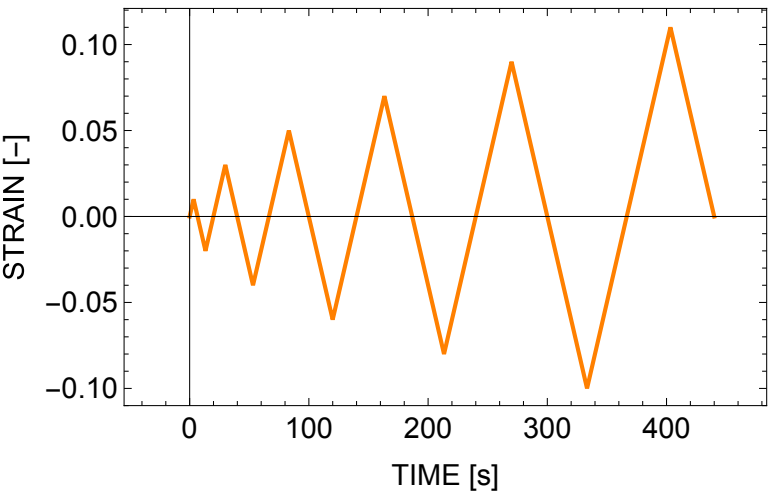

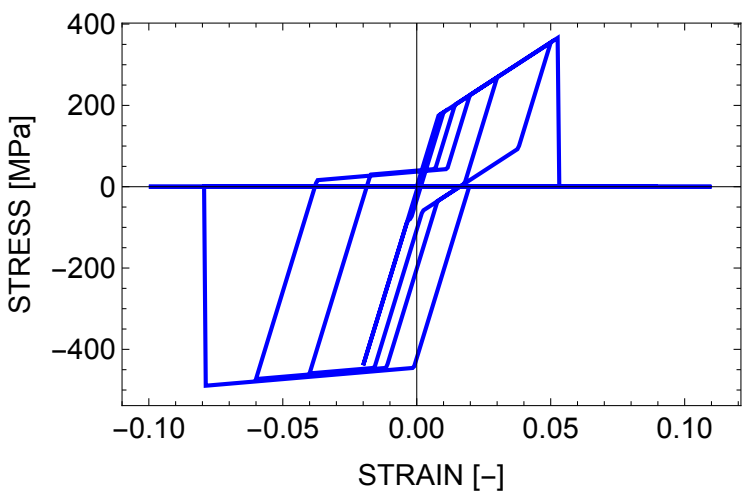

Figure
Click here to download Figure: Fig3.eps

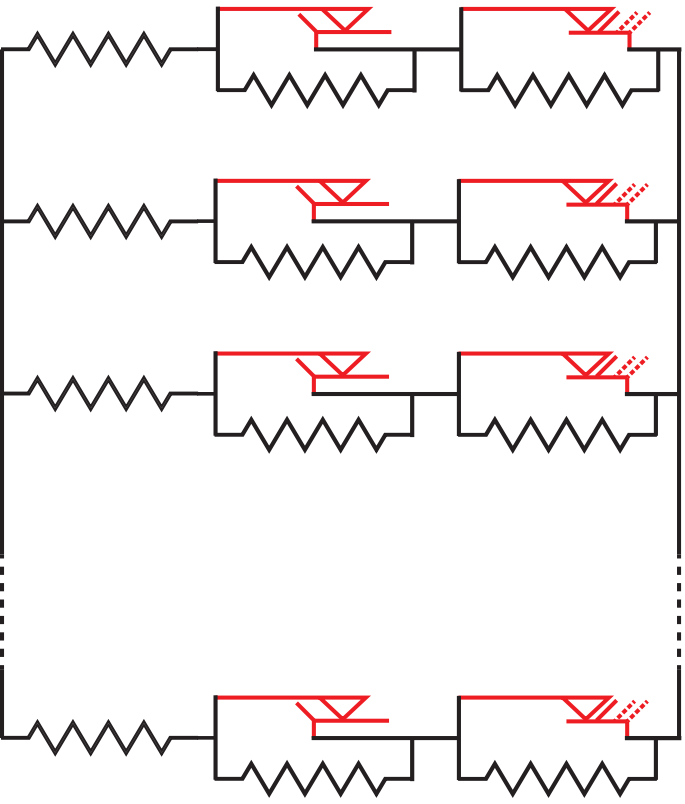

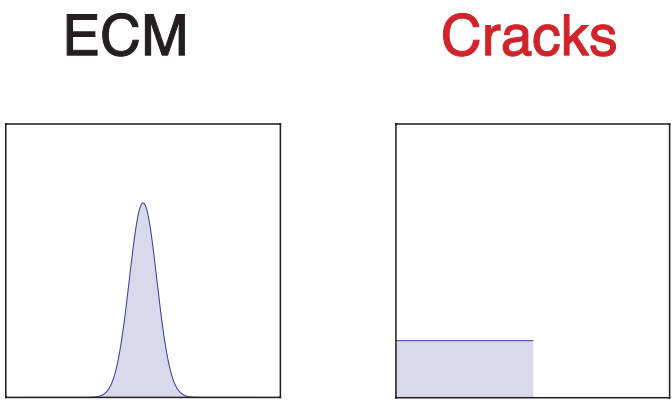

Figure
Click here to download Figure: Fig4.eps

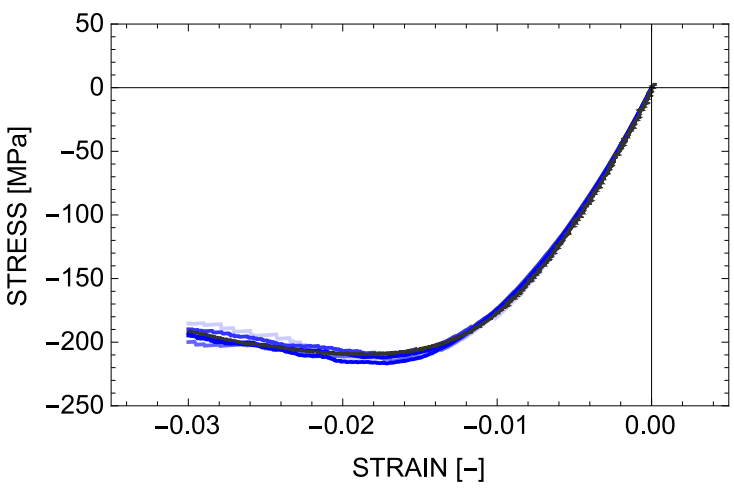

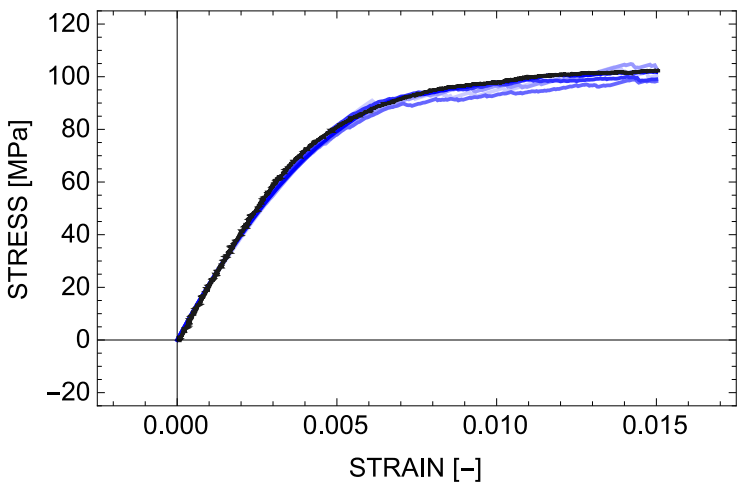

Figure
Click here to download Figure: Fig5.eps

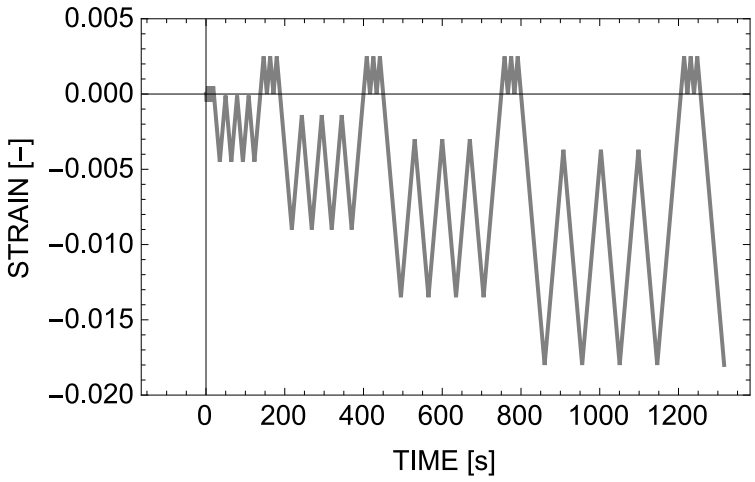

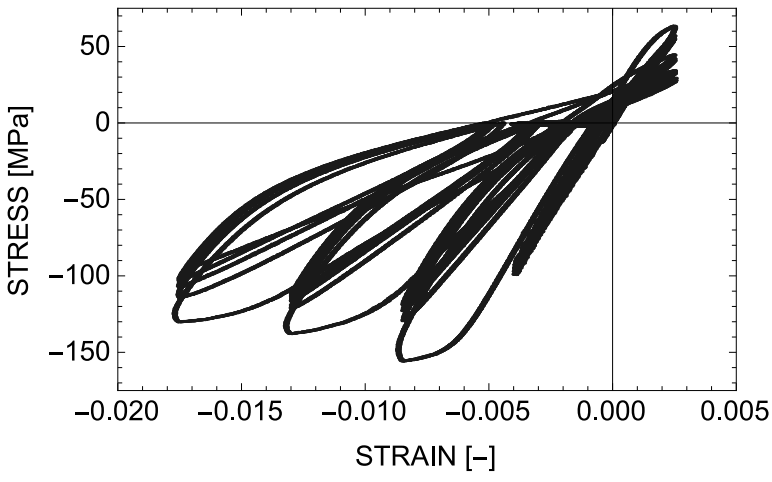

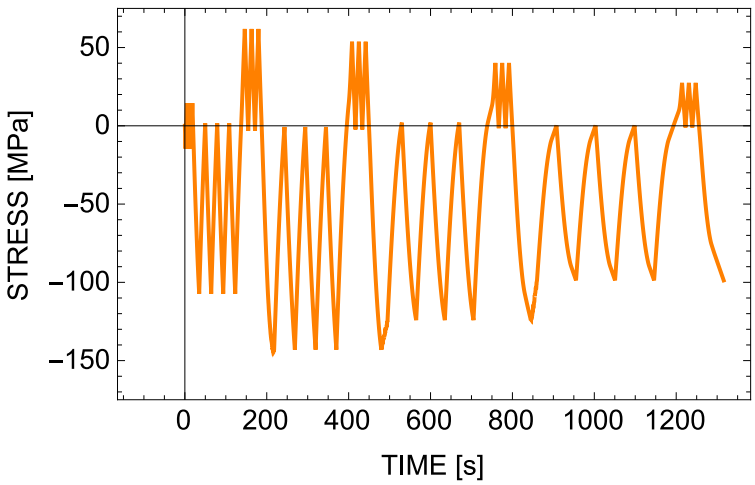

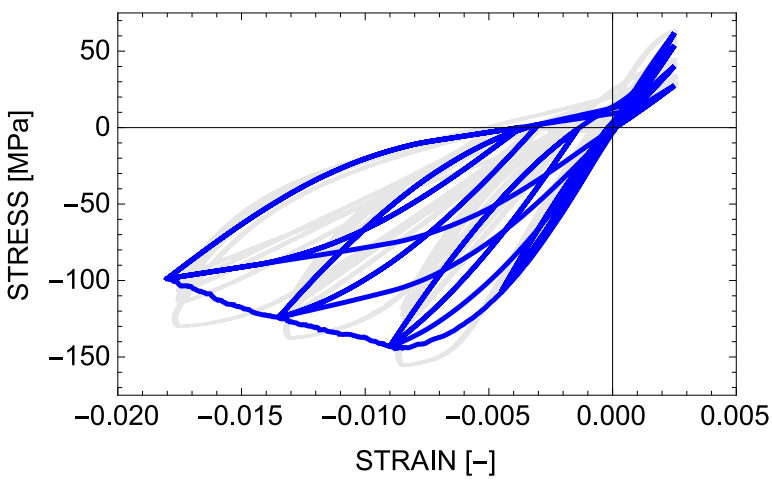

Figure
Click here to download Figure: Fig6.eps

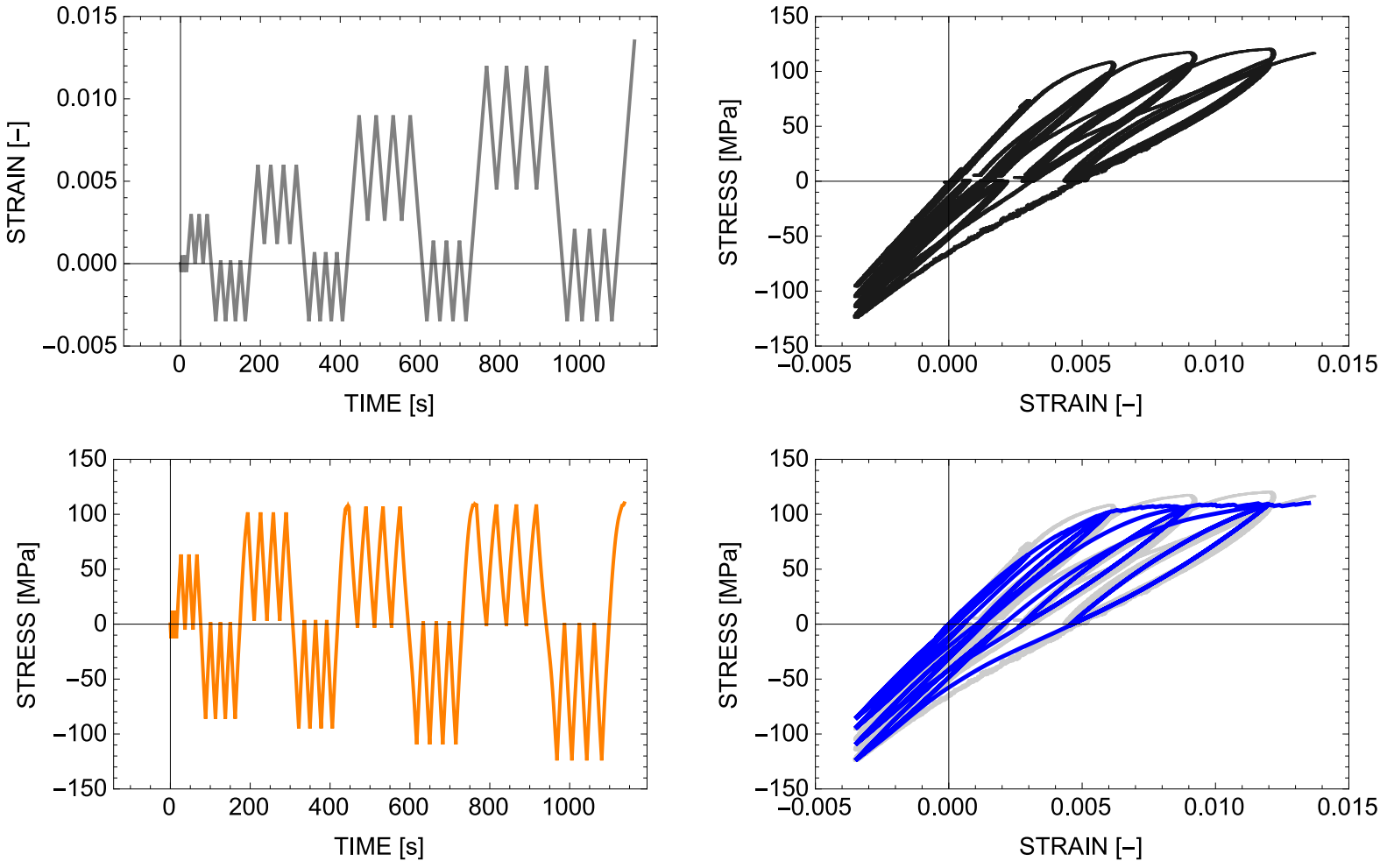

Figure
Click here to download Figure: Fig7.eps

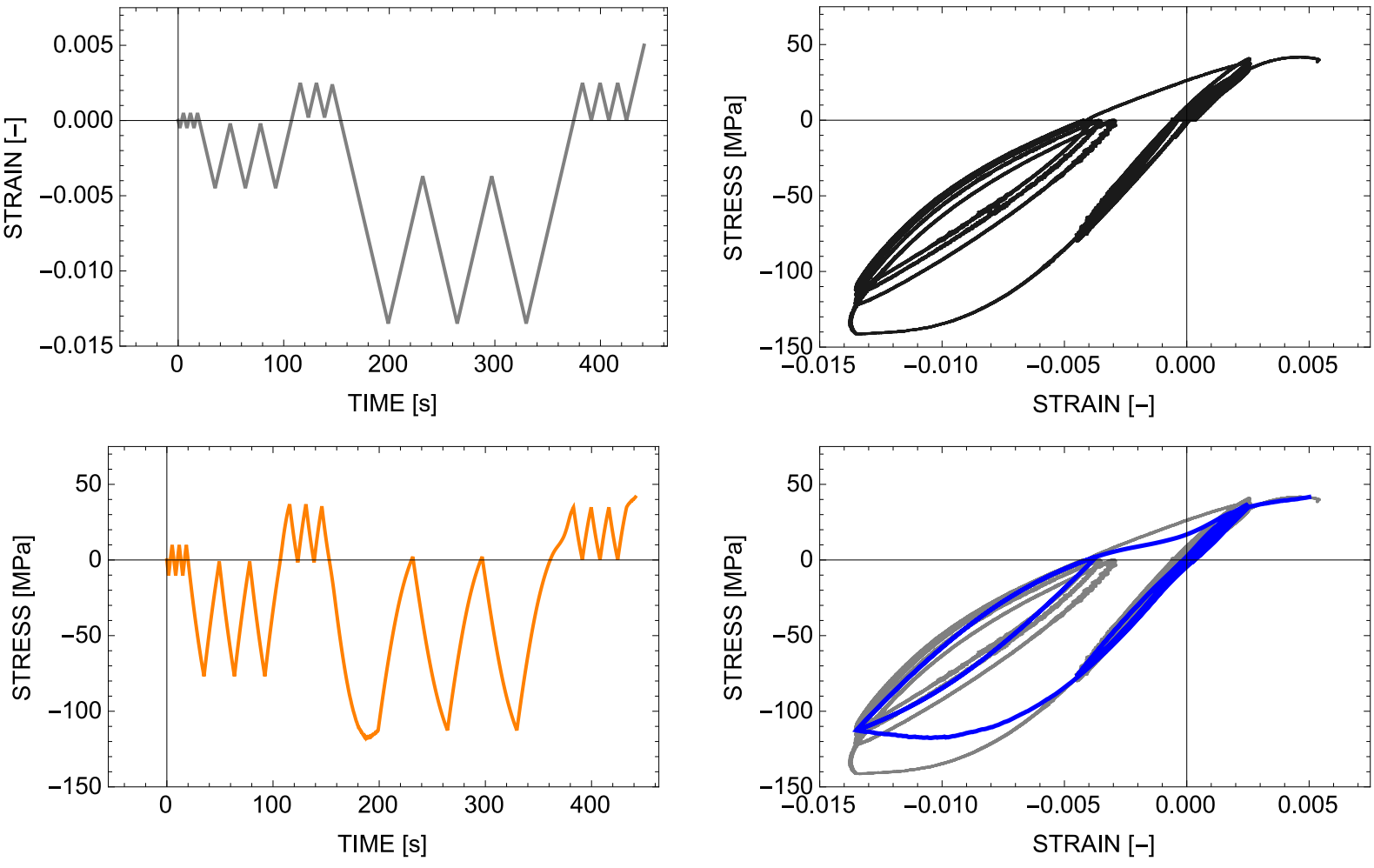

Figure
Click here to download Figure: Fig8.eps